UC Irvine
UC Irvine Previously Published Works

Title

Enhancing oxygen transport in the ionomer film on platinum catalyst using ionic liquid additives.

Permalink

https://escholarship.org/uc/item/68x7d302

Journal

Fundamental Research, 2(2)

ISSN

2667-3258

Authors

Fan, Linhao

Wang, Yun

Jiao, Kui

Publication Date

2022-03-01

DOI

10.1016/j.fmre.2021.09.004

Copyright Information

Peer reviewed
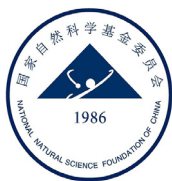
Article

Enhancing oxygen transport in the ionomer film on platinum catalyst using ionic liquid additives

Linhao Fan [a,b], Yun Wang [b,*], Kui Jiao [a,*]

[a] *State Key Laboratory of Engines, Tianjin University, 135 Yaguan Road, Tianjin 300350, China*
[b] *Renewable Energy Resources Laboratory, Department of Mechanical and Aerospace Engineering, University of California, Irvine, CA, 92697-3975, USA*

ARTICLE INFO

ABSTRACT

The O_2 permeation barrier across the nanoscale ionomer films on electrocatalysts contributes to a major performance loss of proton exchange membrane (PEM) fuel cells under low Pt loading. Enhancing O_2 transport through the ionomer films is essential for developing low Pt loading catalyst materials in high-performance PEM fuel cells. This study found that adding an ionic liquid (IL) can effectively mitigate the dense ionomer ultrathin sublayer formed on the Pt surface, which severely hinders O_2 transport to the catalyst sites. The molecular dynamics simulation results show that adding the IL significantly alters the ionomer ultrathin sublayer structure by inhibiting its tight arrangement of perfluorosulfonic acid chains but scarcely impacts the ultrathin sublayer thickness. Additionally, the IL addition provides a larger free space for O_2 dissolution in the ultrathin sublayer. Consequently, due to IL molecules' presence, the O_2 density in the ultrathin sublayer on the Pt surface is improved by an order of magnitude, which will benefit the catalytic efficiency, and the O_2 permeation flux across the ionomer film is increased by up to 8 times, which will reduce the O_2 transport loss of the catalyst layer.

1. Introduction

Energy crisis and environmental pollution are two major global problems in the 21st century. Developing renewable energy and green power devices are active research topics [1,2]. The proton exchange membrane (PEM) fuel cell, with high efficiency and low pollution, is regarded as one of the most promising green power devices, attracting considerable attention for many applications, especially the transportation sector [3-5]. In recent years, fuel cell vehicles (FCVs) have successfully been commercialized with a stack power density as high as 4.4 kW L^{-1} [1]. However, the stack power density is still much less than the target, i.e., 9.0 kW L^{-1} by 2040, according to the New Energy and Industrial Technology Development Organization (NEDO) of Japan [1]. Meanwhile, cost is also a major limitation for further FCV commercialization, mainly due to the platinum (Pt) usage in the catalyst layer (CL) [5]. Thus, significant progress on the stack power density under a low Pt loading needs to be made to improve stack performance. The transport loss, especially the oxygen transport loss in the cathode CL under low Pt loading, is a major limiting factor in stack power density improvement [6,7]. Therefore, reducing the oxygen transport loss in CLs is critical to further FCV stack advancement.

In the PEM fuel cells cathode, O_2 molecules are delivered in the gas flow channel and permeate through the gas diffusion layer (GDL) and CL to the Pt surface for the oxygen reduction reaction (ORR). A high O_2 transport resistance was observed, resulting in a considerable performance loss under low Pt loading [8]. The O_2 transport resistance in PEM fuel cells can be experimentally obtained via the limiting current measurement. In measurement, Wang et al. [9] found that the O_2 transport resistance in the ionomer film is much larger than that in the porous structure of CLs and plays a dominant role in fuel cell performance loss under low Pt loading. Nonoyama et al. [10] indicated that the O_2 transport resistance in the CL's ionomer film is significant at low operating temperatures. Choo et al. [11] revealed that the low water uptake in the ionomer film might cause a considerable O_2 transport resistance in the film. Moreover, Owejan et al. [12] found that the ionomer film's O_2 transport resistance depends on both Pt surface area and particle dispersion. Besides, several molecular dynamics (MD) studies investigated the O_2 permeation phenomena in the ionomer film on the Pt surface [13-15], showing that there exists a dense ionomer ultrathin sublayer near the Pt surface, which is the primary cause for the observed high O_2 transport resistance. For polyhedral Pt nanoparticles, it was shown that O_2 molecule permeation in the ionomer film is much easier near the particle corners and edges than that on the particle facets due to the less dense structure near the corners and edges [16].

Adding ionic liquid (IL) to the Pt electrocatalyst surface was reported to enhance the ORR activity, thus attracting much research attention [17-19]. The observed improvement is found to be likely

---

* Corresponding authors.
E-mail addresses: yunw@uci.edu (Y. Wang), kjiao@tju.edu.cn (K. Jiao).

due to the inhibition of the Pt oxidation and the adsorption of non-reactive species [20-22] by using the rotating disk electrode technique. [MTBD][beti] ([7-methyl-1,5,7-triazabicyclo[4.4.0]dec-5-ene][bis(perfluoroethylsulfonyl)imide]) is a protic and hydrophobic IL, which has a large O_2 solubility relative to other ILs. Li et al. [23] found that the [MTBD][beti] addition in CLs can improve electrocatalyst durability by suppressing the decrease of the electrochemical surface area due to Pt nanoparticle growth and dissolution. They also indicated that [MTBD][beti] could suppress the specific adsorption of the sulfonate groups in Nafion® to the Pt surface, which mitigates the detrimental impact of Nafion® on the ORR activity [24]. Huang et al. [21] compared several types of ILs and found that the [MTBD][beti] IL shows better improvement in the ORR activity. However, excess IL will block the CL pores, affecting reactant transport and reducing the ORR activity in CLs [21,23]. Thus, a thin IL layer coating on the electrocatalyst may be preferable to enhance the ORR activity and electrocatalyst durability without blocking the reactant transport in CL pores [23]. Moreover, Snyder et al. [25] fabricated a CL with [MTBD][beti] addition, and found that the [MTBD][beti] addition increases the reactant concentration and residence time on the catalytic surface and thus enhances the attempt frequency and probability of reaction, resulting in a higher cell performance.

Although several groups have attempted to investigate the impacts of ILs on the electrocatalyst performance, few have proposed MD studies, a powerful tool to investigate nanoscale processes, to explore the fundamentals regarding the IL's effects, such as IL's impacts on the film structure and O_2 density and permeation in the ionomer film of CLs, providing that the O_2 transport resistance in the ionomer film can be a significant limiting factor in CL performance under low Pt loading. In this study, we carried out one of the first MD studies to investigate the film structure and O_2 transport in CL's ionomer film when adding a typical IL, [MTBD][beti], to the catalyst-ionomer interface.

2. Methods

2.1. Molecular structures and models

The chemical structures of perfluorosulfonic acid (PFSA), [MTBD], [beti], water, and hydronium molecules are shown in Fig. 1. Each side chain of PFSA molecule has a negative charge, while the hydronium ion has a positive charge. [MTBD] is a cation with a positive charge, while [beti] is an anion with a negative charge. Six layers of Pt (111) with a distance of 2.27 Å between each Pt layer are adopted, as shown in Fig. 1. The simulation box sizes are set as 6.66 and 6.73 nm in the X and Y directions, respectively, to maintain Pt layers' perfect structure under the periodic boundary condition. The PFSA molecules are modeled by the modified DREIDING force field [26], while the [MTBD][beti] by the OPLS-AA force field [27-29]. The models of the water molecules, hydronium ions, O_2 molecules, and Pt atoms are taken from [30-33]. The potential energy of the bond stretching, bond angle bending, dihedral torsion, van der Waals, and long-rang electrostatic potentials is considered in this study. The model parameters are listed in Tables S1-S3. All MD simulations are performed using the large-scale atomic/molecular massively parallel simulator (LAMMPS) package [34] with a time step of 1.0 fs (see more details in Supplementary Materials). The models of the PFSA molecules, water molecules, hydronium ions, and Pt atoms have been validated in our previous work on O_2 transport in the bulk PFSA and the PFSA film on the Pt surface [13]. Moreover, [MTBD][beti] models are validated by comparing the IL density, O_2 diffusivity, and O_2 solubility in ILs with experimental results (see Supplementary Materials).

2.2. Simulation procedures

The dense ionomer ultrathin sublayer on the Pt surface contributes significant O_2 transport resistance [13-15]. Moreover, the IL coating on
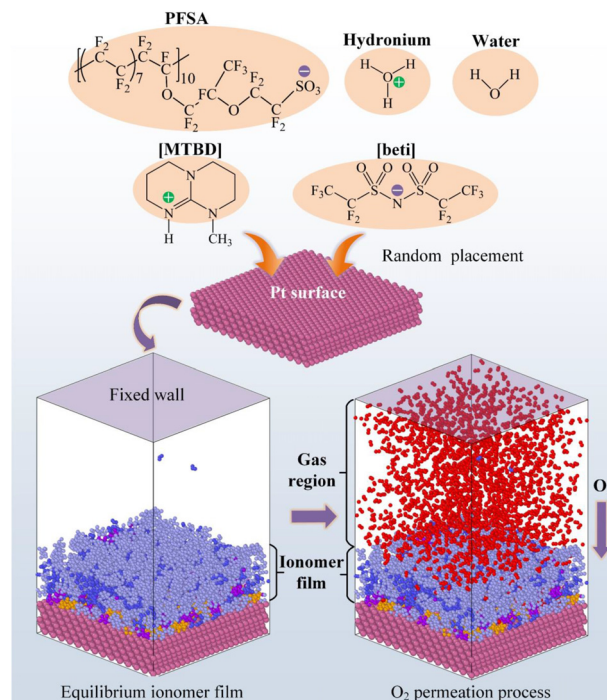

Fig. 1. Schematic of the processes to establish the simulation system.

the electrocatalyst may be preferable to enhance the CL performance [21,24]. Therefore, this study focuses on the IL's impacts on the ionomer structure and O_2 permeation in the region close to the Pt surface. In MD simulation, several [MTBD][beti] molecules are first placed on the Pt surface. Then 8 PFSA molecules, 80 hydronium ions, and several water molecules determined by the water content are randomly inserted into the region above the ILs to obtain the original configuration. After obtaining the original configuration, a series of processes are carried out to get the equilibrium configuration of the ionomer film (see more details in Supplementary Materials). Afterward, 1800 O_2 molecules to ensure enough statistic samples are randomly inserted into the gas region above the equilibrium ionomer film, as shown in Fig. 1. When an O_2 molecule reaches a region within 0.31 nm from the Pt surface, it will be removed from the simulation box, and a new O_2 molecule will be added at the top of the gas region to maintain a constant number of O_2 molecules. A 10 ns NVT simulation at 353 K is performed first to get a steady-state permeation process, followed by another 15 ns NVT simulation at 353 K for analysis.

2.3. Analysis methods

The O_2 solubility (S, cm^3 (standard temperature and pressure, STP) cm^{-3}atm^{-1}) is computed following Widom's test-particle insertion method [35]:

$$S = \frac{T_0}{TP_0}\left\langle \exp\left(\frac{-\Delta E}{k_B T}\right)\right\rangle \tag{1}$$

where P_0 and T_0 are the pressure and temperature at the standard condition ($P_0 = 1.0$ atm, $T_0 = 273.15$ K), respectively; T is the simulation temperature ($T = 353$ K); ΔE is the total potential energy between a test O_2 molecule and other atoms; and k_B is the Boltzmann constant. To obtain the O_2 solubility distribution, the region is divided into 40×40 grids in the X and Y directions, and the distance between two adjacent grids in the Z direction is 0.2 Å. Moreover, 150 configurations are collected from the 15 ns NVT simulation to compute the average solubility.

The free space (d_P, Å) in a point P is defined as the maximum radius of the sphere with point P as its center without overlapping any other

atom:

$$d_P = MIN\langle l_i - 0.5D_i\rangle \tag{2}$$

$$D_i = 2^{1/6}\sigma_i \tag{3}$$

where l_i is the distance of the point P to the atom i; D_i is the atom diameter that is assumed to be the critical distance where the L-J interaction of two atoms transforms from attraction to repulsion; σ_i is the atom L-J parameter in Eq. 1. Computation of the free space distribution is achieved by dividing the region into grids as many as the O_2 solubility distribution.

The radial distribution function (RDF) is the probability of fining B particles at the radius r from A particles, which is expressed as:

$$g_{A-B}(r) = \left(\frac{n_B}{4\pi r^2 dr}\right) / \left(\frac{N_B}{V}\right) \tag{4}$$

where n_B is the number of B particles in the spherical shell with a thickness of dr at the radius r from A particles, $4\pi r^2 dr$ is the shell volume, N_B is the number of B particles in the whole computation region, and V is the volume of the computation region. The data are collected every 2 ps from the 15 ns NVT simulation to compute the RDFs.

The O_2 permeation flux (J, mol s^{-1}m^{-2}) across the ionomer film is defined as:

$$J = \frac{N_O}{N_A A \Delta t} \tag{5}$$

where N_O is the number of oxygen molecules across the ionomer film during the permeation process, A is the area of Pt surface, t is the permeation time (15 ns in this simulation), and N_A is the Avogadro constant. The O_2 flux is obtained by computing the curve slope of the O_2 number across ionomer film as a function of permeation time.

## 3. Results and discussion

3.1. Morphology of ionomer film

The total density distributions in the thickness direction are plotted in Fig. 2a, showing that a dense ionomer ultrathin sublayer (the orange area at ~0-6.8 Å) is present in the ionomer film near the Pt surface due to the strong interaction between Pt and ionomer film. Such a dense ultrathin sublayer was experimentally observed in other studies on the water-metal and electrolyte-metal interface [36-38]. When adding the IL, it becomes less dense with a similar thickness. Moreover, the PFSA and water density distributions in the thickness direction are plotted in Fig. 2b, which shows that when adding the IL, the PFSA density in the ionomer ultrathin sublayer becomes lower, and the water density remains low for both cases with and without the IL. Additionally, the PFSA and water densities are uniform in the middle of the ionomer film, where the interaction strengths significantly decrease due to the longer distance between the Pt and the PFSA and water molecules. The IL addition results in the shift of some PFSA molecules from the ultrathin sublayer to the middle film region, thereby increasing the film thickness. The PFSA density rapidly decreases in the transition region from the ionomer to the gas region, where the water density is almost zero, as shown in Fig. 2b. The [MTBD] and [beti] density distributions in the thickness direction are plotted in Fig. 2c, which shows that the [MTBD][beti] IL mainly exists within the ionomer ultrathin sublayer, and the [MTBD] density is nearly zero at the distance $r > $ ~4.3 Å. Overall, the ionomer film with the IL additives is composed of three regions: the ionomer-Pt interface region (ultrathin sublayer), bulk-like ionomer region (middle film region), and ionomer-gas interface region (upper film region), which is similar to that without the IL [13]. Adding the IL has little impact on the ionomer-Pt interface region's thickness but increases that of the bulk-like ionomer region, as shown in Fig. 2a. The ultrathin ionomer's snapshots with and without the IL are shown in Fig. 2d and

e, respectively. It can be found that the presence of the IL in the ultrathin sublayer mitigates the close arrangement of the PFSA chains on the Pt surface, as shown in Fig. 2e, which will likely affect O_2 permeation. Moreover, the density distributions in the ionomer films' thickness direction with 10 and 30 IL molecules at the water content $\lambda = 7$ and 20 IL molecules at the water content $\lambda = 11$ are illustrated in Fig. S3, which shows similar structural properties.
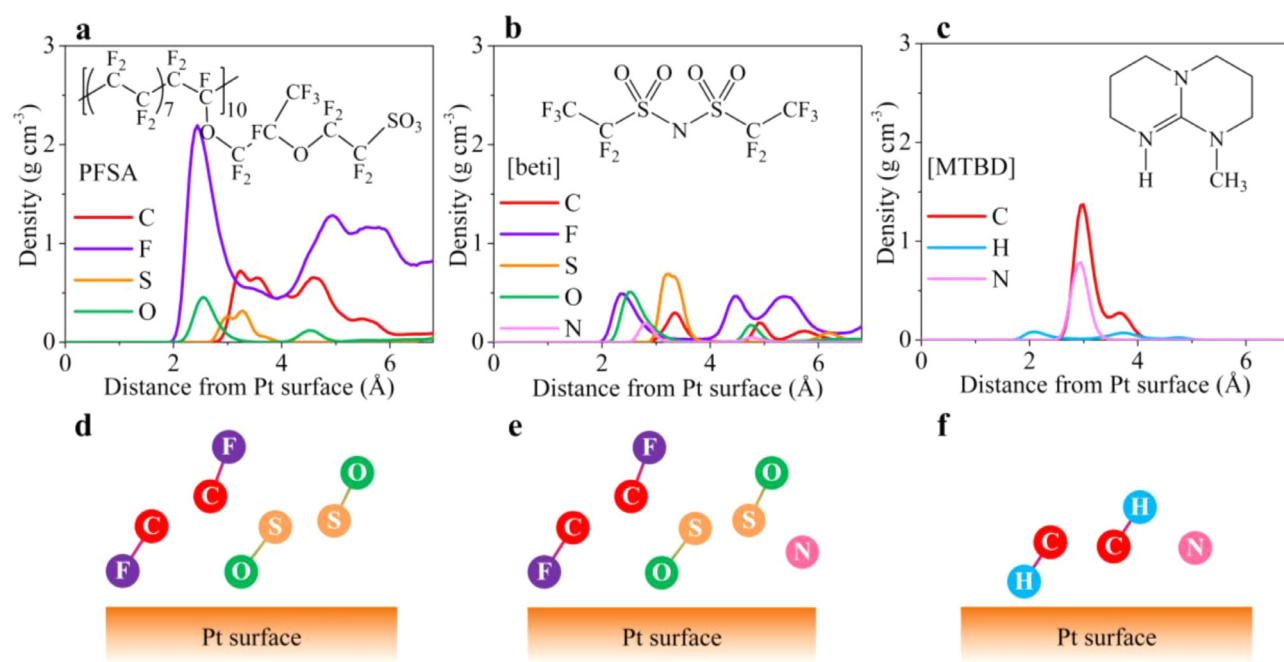
To investigate the atom arrangement in the ionomer ultrathin sublayer, the density distributions of the different types of atoms in the PFSA, [beti], and [MTBD] molecules in the thickness direction are computed and plotted in Fig. 3a-c. As shown in Fig. 3a, the C atoms' density peak location is in the middle of that of the F atoms in the CF_x groups for the PFSA molecules. Similarly, the S atoms' density peak location is in the middle of that of the O atoms in the SO_x groups for the PFSA molecules. The [beti] molecules show similar atom distribution characteristics as the PFSA molecules, as plotted in Fig. 3b. As for the [MTBD] molecules, the C atoms' density peak location is in the middle of that of the H atoms in the CH_x groups, as shown in Fig. 3c. The schematics of the atom arrangements for these molecules are shown in Fig. 3d-f. Moreover, the H atoms in the [MTBD] molecules are closer to the Pt surface than the F atoms in the PFSA and [beti] molecules due to the smaller radius of H than that of F. [MTBD] is a conjugated molecule with coplanar backbone. The C/N atoms in [MTBD] backbone show a significant density peak as shown in Fig. 3c, which means that the coplanar backbone of [MTBD] is nearly parallel to the Pt surface. However, the C atoms in [beti] show two density peaks as shown in Fig. 3b, meaning that the [beti] chain is not aligned closely on the Pt surface. The C atoms in [MTBD] backbone are closer to the Pt surface than that in [beti] and PFSA backbone according to the density distribution as shown in Fig. 3a-c, due to the stronger interaction between [MTBD] and Pt. Consequently, the [MTBD] density is nearly zero at ~4.3-6.8 Å, where the PFSA and [beti] densities are well above zero mainly due to the presence of F atoms. Moreover, the atom density distributions in the thickness direction of the ionomer films with 10 and 30 IL molecules at the water content $\lambda = 7$ and 20 IL molecules at the water content $\lambda = 11$ are illustrated in Figs. S4-S6, which show similar results.
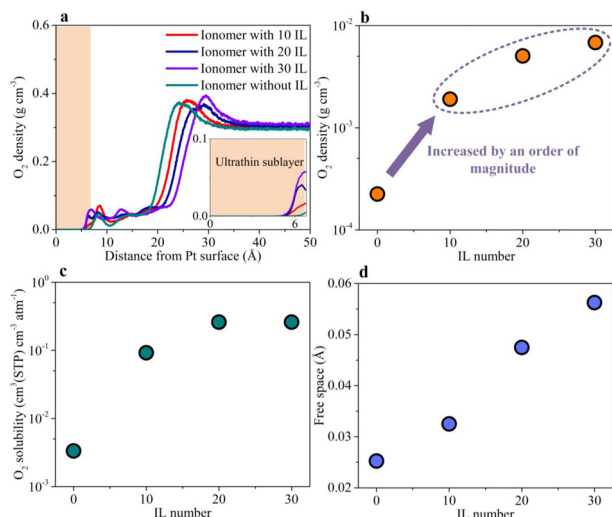
3.2. O_2 density

The O_2 density distributions in the thickness direction of the ionomer films with 0, 10, 20, and 30 IL molecules are plotted in Fig. 4a. An O_2 density peak is present at ~20-30 Å from the Pt surface, where the ionomer density is low, as shown in Fig. 2, for all the ionomer films due to the interaction between the ionomer and O_2 molecules. The density peak location moves away from the Pt surface as the IL number increases due to the increased ionomer film thickness, as shown in Fig. 2. The O_2 density decreases when approaching the Pt surface due to the rapid increase of ionomer density, and it becomes extremely low in the ionomer ultrathin sublayer due to the relatively highly dense structure, thereby resulting in a high O_2 transport resistance as indicated in previous studies [13-15]. The IL mainly exists within the ionomer ultrathin sublayer as shown in Fig. 2c, where the O_2 density distribution is more likely affected. When adding the IL, the O_2 density in the ultrathin sublayer becomes higher and increases as the IL number increases, as shown in Fig. 4b, with the average O_2 density an order of magnitude higher than that without IL additives. Furthermore, the O_2 density distributions in the ultrathin sublayers with 10, 20, and 30 IL molecules at the water content $\lambda = 11$ are plotted in Fig. S7. The figure also shows an increasing trend as the IL number increases. Moreover, the average O_2 solubility and free space at the 4.3-6.8 Å distance from Pt surface are also computed, where the O_2 density is higher as shown in the subfigure in Fig. 4a. Fig. 4c shows that the O_2 solubility in the ultrathin sublayer with IL additives increases with the increasing IL number and is significantly higher than that without the IL. Similarly, the free space shown in Fig. 4d also increases with the increase of IL number. Therefore, the IL additives migrate the close arrangement of PFSA molecules and provide
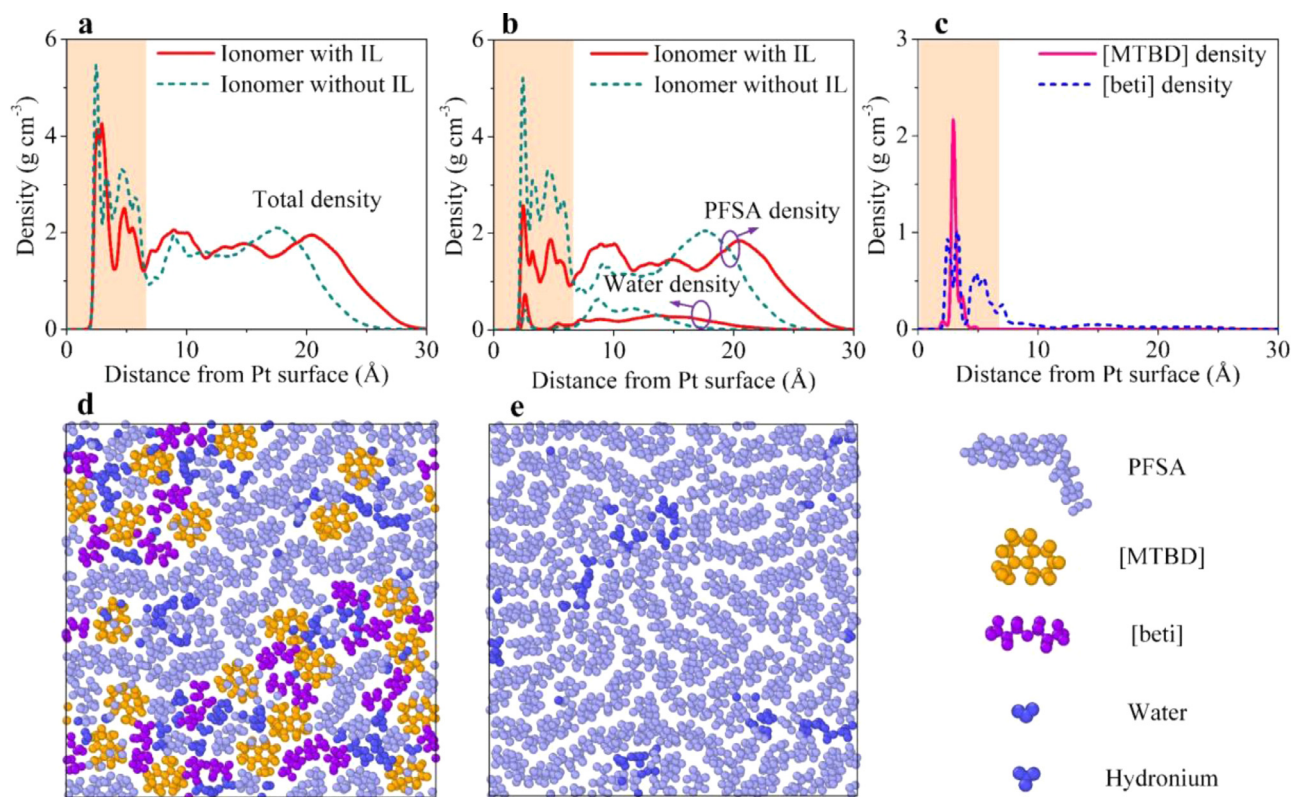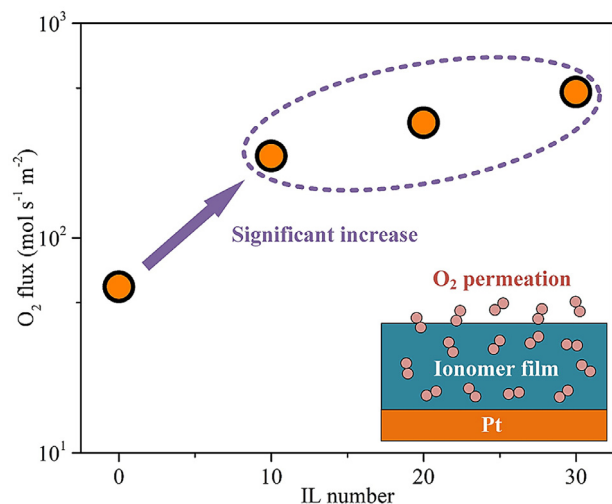
Fig. 2. (a) Total, (b) PFSA and water, (c) [MTBD] and [beti] density distributions in the thickness direction of the ionomer films with 20 IL molecules and without the IL at the water content $\lambda = 7$; and snapshots of the dense ionomer ultrathin sublayer (orange area in a-c) with (d) 20 IL molecules and (e) without the IL. The water content is the number ratio of the water molecules and hydronium ions to the sulfonic acid groups in PFSA.

Fig. 3. Density distributions of the different types of atoms in the (a) PFSA, (b) [beti], and (c) [MTBD] molecules in the thickness direction, and schematics of the atom arrangement of (d) PFSA, (e) [beti], and (f) [MTBD] molecules in the ionomer ultrathin sublayer with 20 IL molecules at the water content $\lambda = 7$.

Fig. 4. (a) O$_2$ density distribution in the thickness direction, (b) average O$_2$ density in the ultrathin sublayer, (c) average O$_2$ solubility, and (d) free space at 4.3-6.8 Å from the Pt surface in the ionomer films with 10, 20, 30 IL molecules and without the IL at the water content $\lambda = 7$.
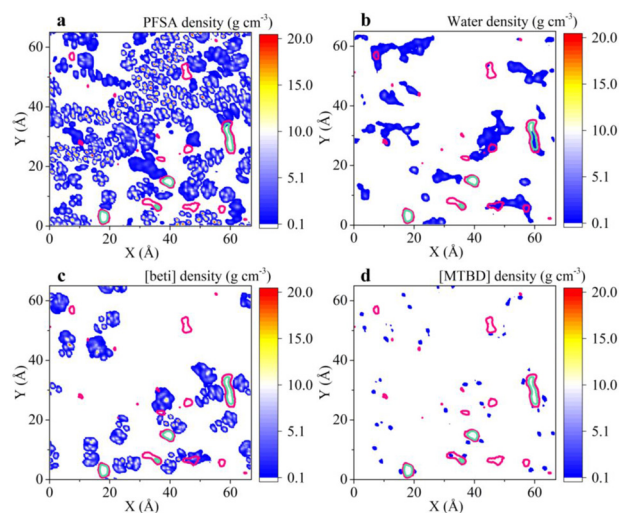

Fig. 6. Two-dimensional density distributions of the (a) PFSA, (b) water, (c) [beti], (d) [MTBD], and O$_2$ molecules in the region at a distance of 4.3-6.8 Å from the Pt surface for the ionomer film with 20 IL molecules at the water content $\lambda = 7$. The red and green lines represent the O$_2$ density contours at 0.1 and 0.5 g cm^{-3}, respectively.

Fig. 5. O$_2$ permeation fluxes across the ionomer films reaching the region at a distance of less than 5.5 Å from the Pt surface for the cases with 10, 20, 30 IL molecules and without the IL at the water content $\lambda = 7$.

a larger free space for O$_2$ dissolution in the ionomer ultrathin sublayer, thereby increasing the O$_2$ density significantly.

3.3. O$_2$ permeation

The O$_2$ permeation fluxes across the ionomer film are also computed. When adding the IL, the O$_2$ flux across the ionomer film becomes higher and increases with the increasing IL number, as shown in Fig. 5. The O$_2$ flux is increased by 4.1, 5.8, and 8.1 times by adding 10, 20, and 30 IL molecules, respectively, in comparison with the case without the IL. The O$_2$ permeation routes are the small cavities at low water contents and the interfacial area between water clusters and PFSA frameworks at high water contents in the middle of the ionomer film (bulk-like region) as indicated in a previous study on the ionomer film without IL addition [13]. The IL additives alter the structure of the ionomer ultrathin

sublayer. Therefore, the O$_2$ permeation routes in the ultrathin sublayer with IL additives are further investigated.

The ionomer ultrathin sublayer is divided into three regions, including the regions at a distance of 0-1.8 Å, 1.8-4.3 Å, and 4.3-6.8 Å from the Pt surface based on the density characteristics. The ionomer density at 0-1.8 Å is nearly zero due to Pt atoms' repulsion, as shown in Fig. 2. The O$_2$ density at 1.8-4.3 Å is much lower than that at 4.3-6.8 Å, as shown in Fig. 4. The two-dimensional density distributions of the PFSA, water, [beti], [MTBD], and O$_2$ molecules at a distance of 4.3-6.8 Å from the Pt surface are plotted in Fig. 6. The red and green lines in Fig. 6 represent the O$_2$ density contours at 0.1 and 0.5 g cm^{-3}, respectively. As shown in Fig. 6a, c, the O$_2$ molecules are mainly in the areas of low PFSA and [beti] density, indicating that the O$_2$ molecules are difficult to dissolve in the PFSA and [beti] domains of the ionomer ultrathin sublayer. A portion of O$_2$ molecules is present in the high-water-density area, as shown in Fig. 6b, which was also observed in the previous study [13]. The water sites provide the main paths for O$_2$ permeation through the ionomer ultrathin sublayer in the IL's absence. Additionally, the [MTBD] density is nearly zero at 4.3-6.8 Å, as shown in Fig. 6d, which possibly provides the paths for O$_2$ transport.

The two-dimensional [MTBD] density distribution at a distance of 1.8-4.3 Å and O$_2$ density distribution at the adjacent location, a distance of 4.3-6.8 Å from the Pt surface, are shown in Fig. 7a. The red and green lines in Fig. 7a represent the O$_2$ density contours at 0.1 and 0.5 g cm^{-3}, respectively. It can be found that most of the O$_2$ molecules at the 4.3-6.8 Å distance exist in the area right above that most [MTBD] molecules are present at the 1.8-4.3 Å distance, where the ionomer density is low as shown in Fig. 6. Furthermore, the O$_2$ solubility and free space distributions at the 4.3-6.8 Å distance from the Pt surface are computed and plotted in Fig. 7b, c. The red lines in Fig. 7b, c represent the O$_2$ solubility contour at 0.77 cm^3 (STP) cm^{-3}atm^{-1} and the free space contour at 0.25 Å, respectively. It can be inferred that, in the region right above the area where most [MTBD] molecules exist, the larger free space due to the lower ionomer density results in a higher O$_2$ solubility, thereby increasing the O$_2$ density in the ionomer ultrathin sublayer. Moreover, the RDFs in the ionomer ultrathin sublayer between the O$_2$ molecules and the C atoms of the PFSA, [MTBD], and [beti] molecules or the O atoms of the water molecules are plotted in Fig. 7d. The peak of the RDF between the O$_2$ molecules and the C atoms of the [MTBD] molecules is
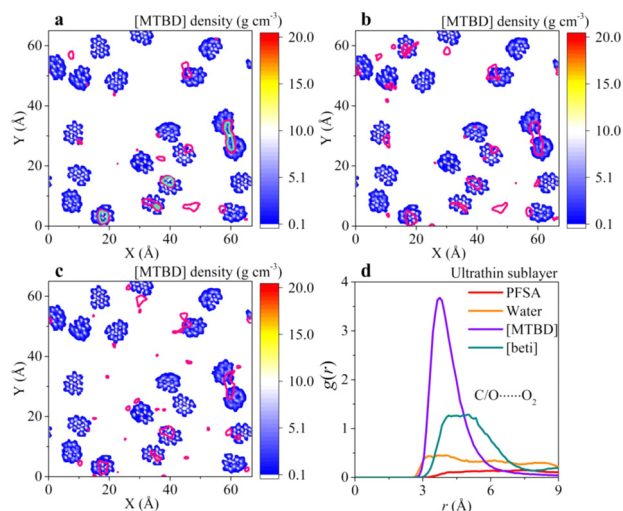
Fig. 7. Two-dimensional [MTBD] density distribution (a-c) in the region at a distance of 1.8-4.3 Å from the Pt surface, (a) two-dimensional O_2 density distribution, (b) O_2 solubility, and (c) free space in the region at a distance of 4.3-6.8 Å from the Pt surface, and (d) RDFs in the ionomer ultrathin sublayer (0-6.8 Å from the Pt surface) for the ionomer film with 20 IL molecules at the water content $\lambda = 7$. The red and green lines in (a) represent the O_2 density contours at 0.1 and 0.5 g cm^{-3}, respectively, while the red lines in (b) and (c) represent the O_2 solubility contour at 0.77 cm^3 (STP) cm^{-3}atm^{-1} and the free space contour at 0.25 Å, respectively. The red, orange, purple, and green lines in (d) represent the RDFs between the O_2 molecules and the C atoms in PFSA, O atoms in water, C atoms in [MTBD], and C atoms in [beti], respectively.

the highest, while that between the O_2 molecules and the C atoms of the PFSA molecules is the lowest, indicating that the O_2 molecules in the ultrathin sublayer are closer to the IL than PFSA molecules. Therefore, the main permeation route of oxygen molecules in the ionomer ultrathin sublayer is inferred to penetrate the IL domain instead of the PFSA domain, thereby enhancing the O_2 transport across the ionomer film when adding the IL. Moreover, the two-dimensional density, O_2 solubility, and free space distributions and the RDFs for the ionomer films with 10 and 30 IL molecules at the water content $\lambda = 7$ and 20 IL molecules at the water content $\lambda = 11$ are illustrated in Figs. S8-S10, which also show similar results.

4. Conclusion

In this study, all-atom MD simulations were performed to investigate the impacts of the [MTBD][beti] IL additives on the film structure and O_2 density and permeation in the ionomer film on the Pt surface. The simulation results showed that adding the IL mitigates the formation of the dense ionomer ultrathin sublayer in the ionomer film near the Pt surface with an overall density less than that without IL addition. The IL addition has little impact on the ultrathin sublayer's thickness but increases that of the bulk-like ionomer region in the middle of the ionomer film. Additionally, adding the IL significantly alters the ionomer ultrathin sublayer structure, i.e., the molecules in the ultrathin sublayer are rearranged upon the IL presence, effectively mitigating the close arrangement of PFSA molecules on the Pt surface. By investigating the atom arrangements of PFSA, [beti], and [MTBD] in the ionomer ultrathin sublayer, we found that the [MTBD] molecules are closer to the Pt surface than the PFSA and [beti] molecules due to the coplanar conformation and stronger interaction with Pt layers. The [MTBD] density was found to decrease to nearly zero near the upper region of the ultrathin sublayer, where the PFSA and [beti] densities subject to little change. Therefore, the O_2 molecules were found to be mainly located above the area where most [MTBD] molecules are present in the

ultrathin sublayer because the low local ionomer density results in the relatively large free space and high O_2 solubility. And the O_2 permeation route is inferred to penetrate the IL domain instead of the PFSA domain. Consequently, the O_2 density in the ionomer ultrathin sublayer is improved by an order of magnitude and the O_2 permeation flux across the ionomer film is increased by up to 8 times due to the IL's presence. These results indicate that adding the IL to a Pt surface can effectively mitigate the formation of the closely arranged PFSA molecules, making the ionomer ultrathin sublayer more accessible for O_2 molecules, which is likely the main reason for the mitigation of the detrimental impact of PFSA on the ORR activity as experimentally observed. These findings are valuable for the fundamental understanding of the IL's roles in CLs and advanced CL fabrication.

Declaration of Competing Interest

The authors declare that they have no conflicts of interest in this work.

Supplementary materials

Supplementary material associated with this article can be found, in the online version, at doi:10.1016/j.fmre.2021.09.004.

References

[1] K. Jiao, J. Xuan, Q. Du, et al. , Designing the next generation of proton-exchange membrane fuel cells, Nature 595 (2021) 361–369.
[2] Y. Qiu, Z. Pan, H. Chen, et al. , Current progress in developing metal oxide nanoarrays-based photoanodes for photoelectrochemical water splitting, Sci. Bull. 64 (2019) 1348–1380.
[3] T. Asset, P. Atanassov , Iron-nitrogen-carbon catalysts for proton exchange membrane fuel cells, Joule 4 (2020) 33–44.
[4] Z. Niu, R. Wang, K. Jiao, et al. , Direct numerical simulation of low Reynolds number turbulent air-water transport in fuel cell flow channel, Sci. Bull. 62 (2017) 31–39.
[5] Y. Wang, D.F.R. Diaz, K.S. Chen, et al. , Materials, technological status, and fundamentals of PEM fuel cells-A review, Mater. Today 32 (2020) 178–203.
[6] L. Du, V. Prabhakaran, X. Xie, et al. , Low-PGM and PGM-free catalysts for proton exchange membrane fuel cells: Stability challenges and material solutions, Adv. Mater. (2020) 1908232.
[7] A. Kongkanand, M.F. Mathias , The priority and challenge of high-power performance of low-platinum proton-exchange membrane fuel cells, J. Phys. Chem. Lett. 7 (2016) 1127–1137.
[8] R. Sun, Z. Xia, X. Xu, et al. , Periodic evolution of the ionomer/catalyst interfacial structures towards proton conductance and oxygen transport in polymer electrolyte membrane fuel cells, Nano Energy (2020) 104919.
[9] C. Wang, X. Cheng, J. Lu, et al. , The experimental measurement of local and bulk oxygen transport resistances in the catalyst layer of proton exchange membrane fuel cells, J. Phys. Chem. Lett. 8 (2017) 5848–5852.
[10] N. Nonoyama, S. Okazaki, A.Z. Weber, et al. , Analysis of oxygen-transport diffusion resistance in proton-exchange-membrane fuel cells, J. Electrochem. Soc. 158 (2011) B416–B423.
[11] M.J. Choo, K.H. Oh, J.K. Park, et al. , Analysis of oxygen transport in cathode catalyst layer of low-Pt-loaded fuel cells, ChemElectroChem 2 (2015) 382–388.
[12] J.P. Owejan, J.E. Owejan, W. Gu , Impact of platinum loading and catalyst layer structure on PEMFC performance, J. Electrochem. Soc. 160 (2013) F824–F833.
[13] L. Fan, Y. Wang, K. Jiao , Oxygen permeation resistances and routes in nanoscale ionomer thin film on platinum surface, J. Electrochem. Soc. 168 (2021) 014511.
[14] R. Jinnouchi, K. Kudo, N. Kitano, et al. , Molecular dynamics simulations on O_2 permeation through Nafion ionomer on platinum surface, Electrochim. Acta 188 (2016) 767–776.
[15] Y. Kurihara, T. Mabuchi, T. Tokumasu , Molecular dynamics study of oxygen transport resistance through ionomer thin film on Pt surface, J. Power Sources 414 (2019) 263–271.
[16] L. Fan, Y. Wang, K. Jiao , Oxygen transport routes in ionomer film on polyhedral platinum nanoparticles, ACS Nano 14 (2020) 17487–17495.
[17] J. Snyder, T. Fujita, M.W. Chen, et al. , Oxygen reduction in nanoporous metal-ionic liquid composite electrocatalysts, Nat. Mater. 9 (2010) 904–907.
[18] M. Qiao, G. Ferrero, L. Fernandez Velasco, et al. , Boosting the oxygen reduction electrocatalytic performance of nonprecious metal nanocarbons via triple boundary engineering using protic ionic liquids, ACS Appl. Mater. Interfaces 11 (2019) 11298–11305.

[19] Q.C. Tran, V.D. Dao, H.Y. Kim, et al. , Pt-based alloy/carbon black nanohybrid covered with ionic liquid supramolecules as an efficient catalyst for oxygen reduction reactions, Appl. Catal., B 204 (2017) 365–373.

[20] G.R. Zhang, T. Wolker, D.J. Sandbeck, et al. , Tuning the electrocatalytic performance of ionic liquid modified Pt catalysts for the oxygen reduction reaction via cationic chain engineering, ACS Catal 8 (2018) 8244–8254.

[21] K. Huang, T. Song, O. Morales-Collazo, et al. , Enhancing Pt/C catalysts for the oxygen reduction reaction with protic ionic liquids: The effect of anion structure, J. Electrochem. Soc. 164 (2017) F1448.

[22] G.R. Zhang, M. Munoz, B.J. Etzold , Accelerating oxygen-reduction catalysts through preventing poisoning with non-reactive species by using hydrophobic ionic liquids, Angew. Chem. Int. Ed. 55 (2016) 2257–2261.

[23] Y. Li, J. Hart, L. Profitt, et al. , Sequential capacitive deposition of ionic liquids for conformal thin film coatings on oxygen reduction reaction electrocatalysts, ACS Catal 9 (2019) 9311–9316.

[24] Y. Li, S. Intikhab, A. Malkani, et al. , Ionic liquid additives for the mitigation of Nafion specific adsorption on platinum, ACS Catal 10 (2020) 7691–7698.

[25] J. Snyder, K. Livi, J. Erlebacher , Oxygen reduction reaction performance of [MTBD][beti]-encapsulated nanoporous NiPt alloy nanoparticles, Adv. Funct. Mater. 23 (2013) 5494–5501.

[26] T. Mabuchi, T. Tokumasu , Effect of bound state of water on hydronium ion mobility in hydrated Nafion using molecular dynamics simulations, J. Chem. Phys. 141 (2014) 104904.

[27] W.L. Jorgensen, J. Tirado-Rives , Potential energy functions for atomic-level simulations of water and organic and biomolecular systems, Proc. Natl. Acad. Sci. U. S. A. 102 (2015) 6665–6670.

[28] L.S. Dodda, I. Cabeza de Vaca, J. Tirado-Rives, et al. , Ligpargen web server: An automatic OPLS-AA parameter generator for organic ligands, Nucleic Acids Res 45 (2017) W331–W336.

[29] M.T. Nguyen, Q. Shao , Effect of zwitterionic molecules on ionic transport under electric fields: a molecular simulation study, J. Chem. Eng. Data 65 (2019) 385–395.

[30] M. Levitt, M. Hirshberg, R. Sharon, et al. , Calibration and testing of a water model for simulation of the molecular dynamics of proteins and nucleic acids in solution, J. Phys. Chem. B 101 (1997) 5051–5061.

[31] S.S. Jang, V. Molinero, T. Cagin, et al. , Nanophase-segregation and transport in Nafion 117 from molecular dynamics simulations: Effect of monomeric sequence, J. Phys. Chem. B 108 (2004) 3149–3157.

[32] G.W. Wu, K.Y. Chan , Molecular simulation of oxygen on supported platinum clusters, J. Electroanal. Chem. 450 (1998) 225–231.

[33] Q. He, D.C. Joy, D.J. Keffer , Nanoparticle adhesion in proton exchange membrane fuel cell electrodes, J. Power Sources 241 (2013) 634–646.

[34] S. Plimpton , Fast parallel algorithms for short-range molecular dynamics, J. Comp. Phys. 117 (1995) 1–19.

[35] S. Ban, C. Huang, X.Z. Yuan, et al. , Molecular simulation of gas transport in hydrated Nafion membranes: Influence of aqueous nanostructure, J. Phys. Chem. C 116 (2012) 17424–17430.

[36] M.F. Toney, J.N. Howard, J. Richer, et al. , Voltage-dependent ordering of water molecules at an electrode-electrolyte interface, Nature 368 (1994) 444–446.

[37] H. Steinruck, C. Cao, Y. Tsao, et al. , The nanoscale structure of the electrolyte-metal oxide interface, Energy Environ. Sci. 11 (2018) 594–602.

[38] V. Barranco, J. Carpentier, G. Grundmeier , Correlation of morphology and barrier properties of thin microwave plasma polymer films on metal substrate, Electrochimica Acta 49 (2004) 1999–2013.

Linhao Fan is currently a Ph.D. candidate of the Tianjin University. He received his B.S. degree from the Tianjin University in 2016. He has been a joint doctoral student in the University of California, Irvine from 2019 to 2020 funded by China Scholarship Council (CSC). He is interested in the micro/nanoscale phenomena in PEM fuel cells. He has published 10+ papers in international journals, such as ACS Nano.

Kui Jiao is currently a professor in the State Key Laboratory of Engines at the Tianjin University, China. He received his Ph.D. degree of mechanical engineering in 2011 from the University of Waterloo, Canada. His research interest includes fuel cell, battery, thermoelectric generator, turbocharger compressor, etc. He has published one book on fuel cell water and thermal management, and 100+ papers in international journals such as Nature. He severed as the Chair for several international conferences such as International Conference on Energy and AI. He was granted the "National Natural Science Foundation of China – Outstanding Youth Foundation" in 2016, and the "UK Royal Society – Advanced Newton Fellowship" in 2018. He has led 30+ national and industrial projects in China, and provided modeling and design services in development of fuel cell engines for many major automotive fuel cell manufactures such as FAW, SAIC Motor, Sunrise Power, Bosch and Weichai Power. He serves as the Editor of Energy and AI and Associate Editor of International Journal of Green Energy. He also serves as the Vice President of Fuel Cell Engine Division, Chinese Society of Internal Combustion Engine (CSICE).